Numerical Simulations of Melt-Driven Double-Diffusive Fluxes in a Turbulent Boundary Layer beneath an Ice Shelf

Leo Middleton

Department of Applied Mathematics and Theoretical Physics, University of Cambridge, Cambridge, United Kingdom

British Antarctic Survey, Cambridge, United Kingdom

Catherine A. Vreugdenhil

Department of Applied Mathematics and Theoretical Physics, University of Cambridge, Cambridge, United Kingdom

Department of Mechanical Engineering, University of Melbourne, Melbourne, Australia

Paul R. Holland

British Antarctic Survey, Cambridge, United Kingdom

John R. Taylor*

Department of Applied Mathematics and Theoretical Physics, University of Cambridge, Cambridge, United Kingdom

**Corresponding author address:* John Taylor, Centre for Mathematical Sciences, Wilberforce Rd, Cambridge, CB3 0WA.

E-mail: J.R.Taylor@damtp.cam.ac.uk

ABSTRACT

The transport of heat and salt through turbulent ice shelf-ocean boundary layers is a large source of uncertainty within ocean models of ice shelf cavities. This study uses small-scale, high resolution, 3D numerical simulations to model an idealised boundary layer beneath a melting ice shelf to investigate the influence of ambient turbulence on double-diffusive convection (i.e. convection driven by the difference in diffusivities between salinity and temperature). Isotropic turbulence is forced throughout the simulations and the temperature and salinity are initialised with homogeneous values similar to observations. The initial temperature and the strength of forced turbulence are varied as controlling parameters within an oceanographically relevant parameter space. Two contrasting regimes are identified. In one regime double-diffusive convection dominates, and in the other convection is inhibited by the forced turbulence. The convective regime occurs for high temperatures and low turbulence levels, where it is long-lived and affects the flow, melt rate and melt pattern. A criterion for identifying convection in terms of the temperature and salinity profiles, and the turbulent dissipation rate, is proposed. This criterion may be applied to observations and theoretical models to quantify the effect of double-diffusive convection on ice shelf melt rates.

1. Introduction

Ice shelves are the floating extensions of ice sheets, found around Antarctica and Greenland. Regional ocean models of the cavities beneath them are often used to help predict the response of ice shelves to various oceanographic forcings (Holland et al. 2010). To calculate the response of the ice shelf to a given ocean state, the turbulent boundary layer in the upper tens of metres must be parameterised. The parameterisation commonly used in ice shelf cavity models was developed based on observations under sea ice (McPhee et al. 1987), and then adapted for the under ice-shelf environment (Holland and Jenkins 1999). Observations necessary for parameterisation validation were previously minimal. However, ice shelf borehole measurements have recently increased in quantity and quality (Davis and Nicholls 2019; Kimura et al. 2015; Begeman et al. 2018; Jenkins et al. 2010).

Davis and Nicholls (2019) analysed turbulence measurements made beneath the Larsen C Ice Shelf. Temperatures within the cold-water cavity were measured as $-2.01 \pm 0.05°C$ at about 2.6 m below the ice. Davis and Nicholls (2019) found their observations were consistent with the Holland and Jenkins (1999) parameterisation, which assumes a shear-driven boundary layer, where stratification due to basal melting has a minimal effect.

The effects of stratification on turbulence within the ocean boundary layer beneath an ice shelf were examined using a Large Eddy Simulations (LES) in Vreugdenhil and Taylor (2019). They considered a steady flow past a dynamically melting boundary and found that, under strongly stratified conditions, shear-driven turbulence was reduced and even damped out. The parameterisation of McPhee et al. (1987) is based on similar arguments and stratification acts to damp turbulence. Holland and Jenkins (1999) argued that stratification effects in the McPhee et al. (1987) parameterisation have a minimal impact on cold cavity ice shelves, and so need not be included within regional ice cavity models. However, the work of Vreugdenhil and Taylor (2019) suggested that stratification effects may be important even for relatively cold far-field temperatures, especially if the shear turbulence is weak. Many ice shelf cavities, including those that are losing ice mass at the fastest rates (Rignot et al. 2013), are warm water cavities. Here the McPhee et al. (1987) parameterisation, and LES (Vreugdenhil and Taylor 2019), suggest stratification plays a dominant role in the transport of heat and salt through the boundary layer.

Certain observations cannot be explained by the damping effect of stratification. Borehole observations made on the George VI Ice Shelf (Venables et al. 2014; Kimura et al. 2015), found layers (or 'thermohaline staircases') in the temperature and salinity profiles adjacent to the ice. Although layers can form in fluids with a single stratifying component (Phillips 1972), Kimura et al. (2015) argued that the staircases observed beneath George VI Ice Shelf are associated with the difference between the molecular diffusivities of temperature and salinity. Thermohaline staircases can form when one scalar is unstably stratified whilst the other is stably stratified (Radko 2013), and here the melting ice provides a stable salinity profile and an unstable temperature profile. This configuration is called the 'Diffusive Convection Favourable' regime (when the unstable stratifying element is salinity, the regime is called 'Salt Fingering Favourable'). Staircases are a common signature of convection triggered by the difference in diffusivities, however double-diffusive convection may occur without staircase formation. In double-diffusive convection, on average turbulence is generated through the release of potential energy, despite the density increasing with depth. The parameterisation of McPhee et al. (1987) assumes the role of the diffusive buoyancy flux at a melting ice base is to create a stratification that damps turbulence, so the parameterisation will not apply well if turbulent production is dominated by double-diffusive convection. The Kimura et al. (2015) hypothesis was that double-diffusive convection is forced at the ice base, leading to the signature staircases below, and we are primarily concerned with investigating this mechanism.

Kimura et al. (2015) compared the under-ice shelf regime to the laboratory experiment of Martin and Kauffman (1977). In this experiment a block of ice was floated atop a box of salt-water (0 °C and 37.6 ppt salinity). Convection was observed throughout the box that persisted for the length of the experiment (two days). The diffusivity of heat is two orders of magnitude larger than the diffusivity of salt, so a diffusing thermal sublayer will thicken faster than a salt sublayer. In the Martin and Kauffman (1977) experiments the density was dominated by the cooled temperature profile beneath the salt boundary layer, causing a peak in density that triggered convection. The velocity field was not examined in these experiments, however a numerical study of a melting boundary was conducted by Keitzl et al. (2016), where similar convection was observed. The Keitzl et al. (2016) simulations showed convective plumes descending from a region immediately below the salt boundary layer, although here the far-field temperatures were larger, varying between 10 °C and 24 °C. Martin and Kauffman (1977) did not observe staircase formation, however their experimental set-up had no ambient stratification. Turner (1968) observed the progressive formation of staircases when heating a stable salt stratification from below, suggesting staircases may form in a stable stratification when double-diffusive convection is forced by a destabilising flux at the boundary. Kimura et al. (2015) argued that diffusive boundary fluxes as in Martin and Kauffman (1977) and a stable stratification as in Turner (1968) led to the staircases observed beneath George VI Ice Shelf. Following Martin and Kauffman (1977) we will not consider staircase formation, and instead we will seek to understand the response of ice-triggered convection to turbulent mixing.

The experiments and observations described above suggest that double diffusion is potentially important beneath ice shelves. However, it is not clear how double-diffusive convection will interact with turbulence occurring within an ice shelf-ocean boundary layer. In steady state it can be shown (using the three equation model in Section 2b) that double-diffusive convection implies a fresh salinity sublayer (below ~ 4 ppt), which was not observed by Kimura et al. (2015) or Martin and Kauffman (1977), implying the observed double-diffusive convection was transient. Nevertheless, the convection in the experiment of Martin and Kauffman (1977) was long lived, with a salinity sublayer growing on the diffusive time scale for salinity, thickening by 1 cm in around 20 hrs. Gade (1979) noted that by agitating crushed ice within salty water, one could inhibit double-diffusive convection, which otherwise caused the melt water to sink. Gade (1979) argued that convection was inhibited by the low-salinity boundary layer being mixed into the interior, where it had a dominant contribution to the density. The inhibition of double-diffusive convection by turbulence has also been observed in the ocean (Shibley and Timmermans 2019; Guthrie et al. 2013) and in laboratory experiments (Crapper 1976).

Although the observations from George IV Ice Shelf reported by Kimura et al. (2015) showed clear evidence for double-diffusive convection, Venables et al. (2014) noted that some turbulent shear profiles taken beneath George VI Ice Shelf showed low dissipation values concurrent with double-diffusive staircases, while others showed no staircases and high dissipation values. One hypothesis is that double-diffusive convection is suppressed when turbulence exceeds a critical threshold. Inspired by these observations, we will test this hypothesis and investigate double-diffusive convection forced by heat and salt fluxes at the ice boundary in the presence of ambient turbulence.

To investigate double-diffusion within an adjusting ice shelf-ocean boundary layer we use idealised, high-resolution numerical simulations, inspired by field observations. We force ambient turbulence to reach a target dissipation rate similar to measurements beneath George VI Ice Shelf (Venables et al. 2014), then consider the evolution of a dynamically melting boundary under a homogeneous initial condition for temperature and salinity. We vary the far-field temperature and forced dissipation rate across simulations as controlling parameters. The initial condition of uniform scalars is not designed to capture staircase formation, and the focus instead is the interaction between turbulence and double diffusion near the ice base.

Double-diffusive convection will be distinguished from 'stratified turbulence' in this paper using the turbulent vertical buoyancy flux, defined as $\langle w'b' \rangle$, i.e. the correlation between the fluctuating vertical velocity w', where angle brackets denote a horizontal average and primes are departures from this average, and the fluctuating buoyancy $b' = g\alpha T' - g\beta S'$ for g the gravitational acceleration, T the temperature, S the salinity and (α, β) constant coefficients of thermal expansion and haline contraction, respectively. The buoyancy flux determines the energetic contribution of the buoyancy field (through potential energy) to the turbulent kinetic energy (TKE) as described in Section 2c. Negative values imply that the buoyancy flux acts as a sink of TKE, and positive values imply the buoyancy flux increases the TKE. If double-diffusive convection is the dominant mechanism we expect a positive buoyancy flux ($\langle w'b' \rangle > 0$), otherwise stratification will dampen turbulence on average ($\langle w'b' \rangle < 0$). However, turbulent buoyancy flux is a noisy measure of energy exchange, that may locally change sign, as it depends on advection. This motivates dividing potential energy into two parts; an 'available' potential energy (APE), that exchanges energy back and forth with the TKE via $\langle w'b' \rangle$ (advection); and a 'background' potential energy (BPE) that exchanges energy with the APE based on the mixing of the buoyancy field (diffusion) (Winters et al. 1995).

For single component fluids the diffusive energy exchange between APE and BPE is one way, i.e. mixing always acts to increase BPE (Winters et al. 1995). The distinction between APE and BPE is complicated for double-diffusive fluids, as buoyancy gradients can sharpen due to diffusion (Merryfield 2000). However, Middleton and Taylor (2020) applied the APE/BPE framework to double-diffusion, where now diffusion can cause 'un-mixing' i.e. a release of BPE into APE. Middleton and Taylor (2020) obtained a simplified criterion to identify transfers of energy from

BPE to APE (Section 4a), and here we will apply this criterion to quantify the importance of double diffusion in our simulations.

Section 2 outlines our simulation set up, focusing on the simulation geometry, forcing and numerical details of the grid and its relation to the turbulent length scales. In Section 3 we discuss the simulation evolution, considering differences between convective and stable regimes. Then in Section 4 we consider the diapycnal flux in our simulations. First we give a review of the criterion introduced by Middleton and Taylor (2020), then we show that convection in our simulations is caused by a region of negative diapycnal buoyancy flux near the ice base and it is well described using the framework from Middleton and Taylor (2020). The region is also well described by the density ratio and buoyancy Reynolds number, which we formulate into a criterion for the inhibition of double-diffusive convection by externally-forced turbulence. Finally, in Section 5 we apply our criterion to the diffusive solution, providing a point of comparison between our simulations, those of Vreugdenhil and Taylor (2019) and the observations. Concluding remarks are offered in Section 6.

2. Methods

The ocean boundary layer beneath a melting ice shelf is simulated in a rectangular box domain (Figure 1). We use periodic boundary conditions in the horizontal x, y directions and impenetrable conditions in the vertical z direction. Dynamic melting boundary conditions are imposed on the temperature and salinity fields locally across the top surface of the domain, along with a no-slip velocity condition. A no-flux, free slip condition is applied at the base. The simulations are initialised with a homogeneous temperature and salinity, which are restored to initial values below an ‘observation’ region of 2.6 m depth. Isotropic turbulence is forced at length scales larger than the observation region, using a methodology taken from Wang et al. (1996), applied as a forcing term discussed in Section 2a. The mechanical forcing is designed to achieve a prescribed rate of turbulent kinetic energy dissipation, with values chosen similar to George VI Ice Shelf observations. The mechanically forced turbulence is intended to represent processes missing from the simulations, such as shear-driven turbulence, internal wave breaking, or interior double-diffusive convection.

a. Governing Equations

Our simulations solve the incompressible, non-hydrostatic, Boussinesq Navier-Stokes equations, with terms to apply mechanical velocity forcing and far-field scalar relaxation. These equations are

$$\frac{D\boldsymbol{u}}{Dt} = -\frac{1}{\rho_0}\nabla p + \nu\nabla^2\boldsymbol{u} - \frac{\Delta\rho}{\rho_0}g\boldsymbol{k} + \underbrace{\frac{\varepsilon_0\boldsymbol{u}}{\langle\boldsymbol{u}\cdot\boldsymbol{u}\rangle}}_{\text{Mechanical Forcing}}, \tag{1}$$

$$\nabla\cdot\boldsymbol{u} = 0, \tag{2}$$

$$\frac{DT}{Dt} = \kappa_T\nabla^2 T - \underbrace{\frac{1}{\tau_0}(\langle T\rangle - T_\infty)r(z)}_{\text{Far-Field Relaxation}}, \tag{3}$$

$$\frac{DS}{Dt} = \kappa_S\nabla^2 S - \overbrace{\frac{1}{\tau_0}(\langle S\rangle - S_\infty)r(z)}, \tag{4}$$

$$\frac{\Delta\rho}{\rho_0} = -\alpha(T - T_0) + \beta(S - S_0). \tag{5}$$

where $\frac{D}{Dt} = \frac{\partial}{\partial t} + \boldsymbol{u}\cdot\nabla$ is the material derivative for $\boldsymbol{u} = (u,v,w)$ the 3D velocity field with respect to position vector $\boldsymbol{x} = (x,y,z)$ and p pressure. The density is ρ, with $\rho_0 = 1000$ kgm^{-3} the reference density and $\Delta\rho = \rho - \rho_0$. We use $\nu = 1.8\times10^{-6}$ m^{2}s^{-1} as kinematic viscosity, and $g = 9.81$ ms^{-2} as gravitational acceleration. T is the temperature field in °C, with T_0 and T_∞ the reference and far-field temperatures respectively. Likewise S is the salinity field in parts per thousand, with S_0 and S_∞ the reference and far-field salinities. The molecular diffusivities are $\kappa_T = 1.3\times10^{-7}$ m^{2}s^{-1} for temperature and $\kappa_S = 7.4\times10^{-10}$ m^{2}s^{-1} for salt. Finally, the constants

$(\alpha, \beta) = (3.87 \times 10^{-5}\ (^\circ\mathrm{C})^{-1},\ 7.86 \times 10^{-4}\ (\mathrm{ppt})^{-1})$ (Jenkins et al. 2010) are the coefficients of thermal expansion and haline contraction. Within the relaxation term, the angled brackets $\langle \cdot \rangle$ represent a horizontal average and $\tau_0 = 200$ s is the relaxation timescale, chosen based on a far-field velocity scale of ~ 5 cms^{-1} and a domain height ~ 10 m. The term $r(z) = 0.5(\tanh(10 - 2z) + 1)$ ensures that the relaxation term only acts in the far-field and $r \simeq 10^{-4}$ at $z = 2.6$ m. Therefore, the temperature and salinity are not forced at a depth similar to the mooring measurements made beneath the ice at Larsen C Ice Shelf and George VI Ice Shelf. Our simulations do not include the effect of Earth's rotation since the non-relaxed part of our domain is small (2.6 m) and there is no mean flow, so rotational effects will be weak. We explain the mechanical forcing term in Section 2c.

b. Simulations Details

Eqns. 1-5 are discretised using a pseudo-spectral method in the horizontal, and a second order finite difference scheme in the vertical (see Taylor 2008). The 2/3 de-aliasing technique (Orszag 1971) is applied whereby the Fourier coefficients associated with the largest $\frac{1}{3}$ of wavenumbers are set to zero. This has the effect of dissipating scalar variance on scales smaller than 3Δ, where Δ is the horizontal grid spacing. In regions of the flow where the simulations do not resolve the Batchelor scale, the de-aliasing procedure and the numerical dissipation associated with the finite difference scheme acts like an implicit subgrid-scale model by removing small-scale variance. An implicit Crank-Nicholson method is used to time-step the viscous and diffusive terms, and a third order Runge-Kutta method for other terms.

Full details on the melt condition can be found in Vreugdenhil and Taylor (2019), however in summary, the method solves the diffusive three equation model (Frank 1950) at the boundary, i.e.

the equations

$$\rho_i L_i m = c_p \rho_w \kappa_T \frac{\partial T}{\partial z}\bigg|_b, \tag{6}$$

$$\rho_i S_b m = \rho_w \kappa_S \frac{\partial S}{\partial z}\bigg|_b, \tag{7}$$

$$T_b = \lambda_1 S_b + \lambda_2 + \lambda_3 P, \tag{8}$$

where m is the melt rate, T_b is the temperature at the ice base, and S_b is the salinity at the ice base. The constants are $c_p = 3974\ \mathrm{m^2s^{-2}kg^{-1}(^\circ C)^{-1}}$ for specific heat capacity, $L_i = 3.35 \times 10^5\ \mathrm{m^2s^{-2}kg^{-1}}$ for latent heat of fusion and $\rho_w = 1000\ \mathrm{kgm^{-3}}$, $\rho_i = 920\ \mathrm{kgm^{-3}}$ for the densities of seawater and ice respectively. Here $\lambda_1 = -5.73 \times 10^{-2}\ ^\circ\mathrm{C}$, $\lambda_2 = 8.72 \times 10^{-2}\ ^\circ\mathrm{C}$ and $\lambda_3 = -7.53 \times 10^{-4}\ ^\circ\mathrm{Cdbar^{-1}}$ (Jenkins et al. 2010). The gradients $\frac{\partial S}{\partial z}$ and $\frac{\partial T}{\partial z}$ are calculated at the boundary, at each time step, in each grid cell, to give a dynamic melt condition. The heat and salt flux through the ice is set to zero, as suggested by Holland and Jenkins (1999). We neglect the volume input of melt water, as the interface moves slowly compared to the turbulent velocities.

Resolving the diffusive length scales for salinity everywhere in the domain is prohibitively expensive as the molecular diffusivity is small. Previous numerical simulations (Gayen et al. 2016) used artificially large diffusivities to resolve double-diffusive behaviour. However, this may lead to under-estimation of the double-diffusive effects. We use realistic molecular diffusivities for temperature and salinity and use a fine grid spacing to resolve the smallest diffusive scales within the scalar sublayers. In the turbulent region beneath these sublayers, turbulent fluxes will dominate heat and salt transport, and so it is sufficient that our simulations resolve the smallest velocity scales within the observation region, $z < 2.6$ m, using typical resolution criteria. In other words, the simulations can be classified as direct numerical simulations (DNS) near the ice where they resolve the scalar and velocity gradients and implicit large-eddy simulations farther from the ice where they resolve the turbulent eddies but not all scales of tracer variance. A similar approach has been used before to simulate turbulent scalar transport of active tracers (e.g. Hickel et al. 2007; Scalo et al. 2012). For further details relating to the grid spacing see Appendix A.

Table 1 lists the simulation runs. These are split into 'warm' simulations (0.15 °C), with temperatures similar to George VI Ice Shelf (Venables et al. 2014), and 'cold' simulations (−2.15 °C) similar to cold-water ice shelves such as Larsen C Ice Shelf (Davis and Nicholls 2019). The warm temperatures are similar to the Martin and Kauffman (1977) experiment. We also consider small far-field temperatures (simulations 3 – 6) to investigate the simulation evolution when stratification is weak. The initial salinity $S_\infty = 34.572$ ppt, the same across simulations, is taken from an average of CTD profiles at 2.6 m depth from George VI Ice Shelf. The temperature and salinity fields are initialised with constant values T_∞ and S_∞ in each simulation. We consider two values of the target dissipation rate, ε_0, as described below in Section 2c.

c. Mechanical Forcing

The mechanical forcing term labeled in Eq. 1 is formulated so, in the absence of convection and buoyancy effects, the mean turbulent dissipation rate will be approximately ε_0. The volume-averaged turbulent kinetic energy (TKE) budget is

$$\frac{\partial k}{\partial t} = \underbrace{-\nu \overline{\frac{\partial u_i'}{\partial x_k}\frac{\partial u_i'}{\partial x_k}}}_{\substack{\text{Rate of}\\ \textit{Turbulent}\\ \text{Dissipation}\\ \varepsilon}} + \underbrace{\overline{w'b'}}_{\substack{\textit{Turbulent}\\ \text{Buoyancy Flux}}} + \underbrace{\varepsilon_0}_{\substack{\text{Mechanical}\\ \text{Forcing}}} \tag{9}$$

where $k = \frac{1}{2}(\overline{(u')^2} + \overline{(v')^2} + \overline{(w')^2})$ is the TKE, an over-bar denotes a volume average, and primes are departures from the volume average. There is an implicit sum over repeated subscripts.

For quasi-steady states, the rate of change of TKE is small. If the buoyancy flux is also small, the dominant energy balance is $\varepsilon \simeq \varepsilon_0$. We will refer to ε_0 as the target dissipation rate. In practice, target values of 1×10^{-10} m^{2}s^{-3} and 2×10^{-9} m^{2}s^{-3} resulted in dissipation rates of

$(8.7 \pm 1.8) \times 10^{-11}$ m^{2}s^{-3} and $(1.7 \pm 0.15) \times 10^{-9}$ m^{2}s^{-3} within the passive spin-up simulation at steady state. The target value of 1×10^{-10} m^{2}s^{-3} is similar to the lower values measured beneath George VI Ice Shelf (Venables et al. 2014) and the forced value of 2×10^{-9} m^{2}s^{-3} is similar to the lower values measured beneath the Larsen C Ice Shelf (Davis and Nicholls 2019).

The turbulent buoyancy flux $\overline{w'b'}$ represents energy transfer between kinetic and potential energy. In steady state, the melt condition and relaxation provide sources of potential energy. When the buoyancy flux is included, the dissipation rate will increase or decrease relative to the equilibrium rate ε_0 depending on the sign of $\overline{w'b'}$.

As in Wang et al. (1996), we only force the lowest wavenumbers and allow the turbulent cascade to form naturally at higher wavenumbers. This method of forcing stratified turbulence has been used extensively by previous authors (Rao and de Bruyn Kops 2011; Taylor and Stocker 2012) to simulate stratified turbulence, including by Taylor et al. (2019) to test the assumptions underlying studies of ocean mixing. Specifically, we force wavelengths greater than $L/2.5$ and less than L, where L is the domain size, following Wang et al. (1996). We want the smallest forced wavelength (i.e. $L/2.5$) to be no smaller than the height of the observation region (2.6 m), which sets the minimum vertical length scale as $L = 2.5 \times 2.6\,\mathrm{m} = 6.5$ m. In the relaxation region we set both the domain width and height equal to the minimum scale of (6.5 m) to achieve an isotropic forcing.

3. Results

a. Flow Regimes

In the case with no forced turbulence, once the scalars are initialised, the sublayers in temperature and salinity begin to grow. The thermal sublayer grows faster than the haline sublayer due to the larger molecular diffusivity of temperature. This leads to a double-diffusive boundary layer structure, comparable to the lower half of a double-diffusive interface (e.g. Carpenter et al. 2012), with a stable 'core' where the salinity dominates the density above a 'diffusive boundary layer' where the temperature dominates the density and leads to a peak in density. This behaviour is reproduced by the diffusive solution for T/S evolution beneath a melting interface from Martin and Kauffman (1977). The peak in density may then become unstable leading to diffusive convection. Figure 2 shows profiles of horizontally-averaged scalar fields for the cold, low mechanical forcing case 2B at various times. The early time behaviour of this simulation is similar to the unforced case and matches the diffusive solution. The plots are magnified to show the peak in mean density, however this variation is a small proportion of the total density difference which is largely contained in the T and S sublayers, as shown in the inset.

The addition of forced turbulence enhances vertical mixing of temperature and salinity, which acts to remove the mid-depth density maximum. As the flow evolves, the density peak increases in depth and decreases in magnitude. Changes in the magnitude of the density peak are sometimes dominated by salinity and sometimes by temperature, and hence cannot be attributed to mixing of one scalar alone. In the warmer simulations 1B, 1C and the unforced simulations 1A, 2A, the decrease in density peak magnitude is slow and the peak persists throughout the simulations (50+ hours in all cases). This suggests that if the conditions are sufficient to trigger convection, it may be long lasting. In the cold, mechanically forced cases (2B, 2C, 3, 4, 5, 6) the mean density profiles do become gravitationally stable during the simulation, with differing transition times dependant on the thermal and mechanical forcing. Case 2B, shown in Figure 2, took the longest of the cold cases to transition; the density profile has a peak in the mean profile until around 200 hrs, although at 100 hrs the peak is not visible without greater magnification. However, the lack of a peak in the mean density profile does not imply that no double-diffusive convection is present. It is possible that the stratification is still adding energy to the TKE via an up-gradient turbulent vertical buoyancy flux as discussed below in Section 4a. Therefore, we use the sign of $\langle w'b' \rangle$ to identify double-diffusive convection.

Figure 3 shows the horizontally-averaged turbulent vertical buoyancy flux $\langle w'b' \rangle$ for three simulations: the warm, low mechanical forcing case 1A; the cold, low mechanical forcing case 2B and the cold, high mechanical forcing case 2C. Positive values of $\langle w'b' \rangle$ indicate that the potential energy is acting as a source of TKE, and negative values indicate that TKE is converted into potential energy. Initially, a region with $\langle w'b' \rangle > 0$ descends through the domain in all cases, due to the density peak discussed above. In the cold, low mechanical forcing cases, there are areas of $\langle w'b' \rangle < 0$ visible after some time. In case 2B these patches are initially confined near the ice base, however at later times they descend throughout the domain. In case 2C the regions quickly develop throughout the domain, however regions of $\langle w'b' \rangle$ are still present, despite not being the dominant contribution to the horizontal average. In the warm case 1B, $\langle w'b' \rangle > 0$ throughout the simulation length (50 hrs), and there are no regions of $\langle w'b' \rangle < 0$ descending through the domain. The mean density profile is relatively effective at determining the sign of $\langle w'b' \rangle$. In case 2C the density profile transitions after ~ 4 hrs, close to the time when $\langle w'b' \rangle$ changes sign (~ 2 hrs). However, there are still regions of $\langle w'b' \rangle > 0$ in case 2C, and in case 2B the changing sign of $\langle w'b' \rangle$ is sufficiently noisy that the direction of energy transfer between APE and TKE is not clear. Some variation in the sign of $\langle w'b' \rangle$ may be attributed to reversible exchanges between potential energy and TKE i.e. 'stirring' (Winters et al. 1995), however double-diffusive effects may also be responsible.

The magnitude of $\langle w'b' \rangle$ is also relevant. When $\langle w'b' \rangle$ is large and positive, it can dominate the TKE budget, but for small values it may not be energetically important. Figure 4 shows a snapshot of the vertical velocity field w for the three simulations 1B, 2B and 2C at $t \sim 2$ hrs. The influence of the descending region of elevated buoyancy flux (see Figure 3) is visible in Figure 4 in case 1B as an elevated value of w close to the ice base that moves down through the domain.

However, in the cold cases 2B and 2C there is no visible contrast in the vertical velocity field. Even when buoyancy flux does not affect the velocity field, preferential diffusion may still affect the evolution of the scalar profiles which determine the melt rate.

In our convecting simulations, the magnitude of $\langle w'b' \rangle$ can be approximated by $g\alpha\langle w'T' \rangle$ away from the ice, which in turn can be approximated using the melt rate (not shown). The dominant mode of scalar transport is the large scale forced eddies, amplified by the convective motions as shown in the warm case in Figure 4. We show that the largest scales are responsible for the majority of the scalar fluxes in Figure 5 by considering the fluxes in wavenumber space. The co-spectrum of the scalar flux is calculated as $\langle \hat{w}\hat{\Theta}^* \rangle$ for scalars Θ, $\hat{\cdot}$ denoting the Fourier transform and * denoting the complex conjugate. We show the turbulent scalar fluxes for $\Theta = b', g\alpha T', g\beta S'$ i.e. the turbulent buoyancy flux, and the thermal and haline components of the turbulent buoyancy flux. The scalar fluxes are averaged between 1 m and 3 m away from the ice, and then integrated between 0 and k, the radial wavenumber. The convergence of the integral in Figure 5 shows that the largest scales are responsible for the majority of the integrated turbulent scalar fluxes, which suggests the details of the smallest scales (which we do not resolve) will have a small effect on the scalar fluxes. We have marked the cutoff frequency k_c in the application of the $2/3$ de-aliasing rule (see Section 2b). The thermal component of the buoyancy flux dominates the buoyancy flux in Figure 5, which holds throughout the convective regime.

b. Melt

Figure 6 shows the horizontally-averaged melt rate as a function of time. The diffusive theory is accurate for early times in all cases. After the diffusive phase, all simulations show an increase in the melt rate due to turbulent mixing. For the cases with persistent convection (i.e. all apart from the cold, high mechanical forcing case 2C), the melt rate continues to decrease as $t^{-1/2}$ after the onset of convection. This can be explained by the fact that the salinity sublayer continues to grow on the diffusive timescale as the diffusive salt flux from the melting boundary is much larger than the turbulent vertical salt flux in the convecting region. On the other hand, the boundary heat flux rapidly comes into balance with the turbulent vertical heat flux (not shown). As the gravitationally stable haline sublayer grows, turbulence is damped out over a larger area close to the ice base, reducing the turbulent vertical heat flux. This leads to a reduction in the boundary heat flux, which coupled with the reduction in the boundary salt flux, reduces the melt rate on the time scale of the growing salinity sublayer. Eventually the boundary diffusive salt flux will come into balance with the turbulent vertical salt flux and the system can reach a steady state. In the cold, high mechanical forcing case 2C, the system has almost reached this steady point near the end of the simulated period.

There is an imprint of convection on the spatial patterns of the instantaneous melt rate, although this effect is limited to cases in which $\langle w'b' \rangle$ is large compared to ε_0 (i.e. warm cases). Figure 7 shows snapshots of the melt rate for three simulations. In the cold case 2C the melt rate follows the patterns of the forced turbulence, illustrated by the passive case. In the warm, low mechanical forcing case 1B, where convection is strong, plume-like structures are visible in the melt rate. We may expect qualitatively different roughness patterns to develop on the underside of ice in the presence of strong double-diffusive convection. However, including feedbacks from a moving boundary would be necessary to test this hypothesis.

4. Diapycnal Buoyancy Flux

In this section we identify a mechanism for the double-diffusive convection discussed within Section 3. We propose that the dominant forcing for double-diffusive convection is a region of negative diapycnal buoyancy flux near the ice base and we locate it based on a criterion given by Middleton and Taylor (2020). We first review the criterion and its motivation in terms of double-diffusive energetics.

a. Background Theory

Here, we define the diapycnal buoyancy flux as the diffusive flux of buoyancy across surfaces of constant buoyancy, or isopycnals. For double-diffusive fluids, the diapycnal buoyancy flux can be up-gradient, which corresponds to a negative buoyancy diffusivity (Radko 2013). The energetics of this was recently described by Middleton and Taylor (2020) as a diffusive release of 'background' potential energy (BPE). Background potential energy is defined as the potential energy associated with an adiabatic rearrangement (i.e. sorting) of the density field, and 'available' potential energy is the remaining potential energy after the background portion is subtracted. Winters et al. (1995) formalised the budget for the BPE for a single scalar, and showed the diapycnal buoyancy flux acts to transfer energy from APE to BPE, and so is associated with 'irreversible mixing' (Winters et al. 1995). Extending the same framework, Middleton and Taylor (2020) showed that, in a double-diffusive fluid, the up-gradient buoyancy flux corresponds to a conversion of BPE into APE which can then be modified into TKE via the turbulent vertical buoyancy flux $\langle w'b' \rangle$.

Middleton and Taylor (2020) provided a criterion for a negative diapycnal buoyancy flux in terms of the 3D scalar gradients. Specifically, the sign of the buoyancy flux is set by the following function,

$$\mathrm{sgn}(\nabla b_p \cdot \hat{\boldsymbol{n}}) = \mathrm{sgn}\left(f\left(G_\rho, \theta, \frac{\kappa_T}{\kappa_S}\right)\right), \tag{10}$$

where $\nabla b_p = g\alpha\kappa_T\nabla T - g\beta\kappa_S\nabla S$ is the diffusive buoyancy flux, $\hat{\boldsymbol{n}} = \nabla b/|\nabla b|$, and hence $\nabla b_p \cdot \hat{\boldsymbol{n}}$ is the diapycnal component of the diffusive buoyancy flux. The polynomial f is

$$f\left(G_\rho, \theta, \frac{\kappa_T}{\kappa_S}\right) = \frac{\kappa_T}{\kappa_S}G_\rho^2 + \left(\frac{\kappa_T}{\kappa_S} + 1\right)G_\rho\cos\theta + 1, \tag{11}$$

where the 'gradient ratio', $G_\rho = \alpha|\nabla T|/\beta|\nabla S|$ is the 3D analogue to the density ratio $R_\rho = \alpha\frac{dT}{dz}/\beta\frac{dS}{dz}$, and θ is the angle formed between the gradient vectors ∇S and $-\nabla T$. When $\theta = 0$ the gradient vectors contribute to the buoyancy gradient constructively, and when $\theta = \pi$ they have opposing contributions to the buoyancy gradient. Negative values of f (and an up-gradient diapycnal buoyancy flux) require $\theta_c < \theta < 2\pi - \theta_c$, where

$$\theta_c = \arccos\left(\frac{-2\sqrt{\frac{\kappa_T}{\kappa_S}}}{\frac{\kappa_T}{\kappa_S} + 1}\right) \sim 98.6^\circ, \tag{12}$$

where the $f < 0$ region is bounded by θ_c and $2\pi - \theta_c$. Generally, an up-gradient diapycnal buoyancy flux is possible when the gradient vectors ∇T and ∇S make opposing contributions to the buoyancy gradient $\nabla b = g\alpha\nabla T - g\beta\nabla S$. The $f < 0$ region is also bounded by $G_\rho = 1$ and $G_\rho = \frac{\kappa_T}{\kappa_S}$ i.e. the salinity gradient must dominate the buoyancy gradient magnitude, but the temperature gradient must dominate the buoyancy flux gradient $\nabla b_p = g\alpha\kappa_T\nabla T - g\beta\kappa_S\nabla S$ magnitude. For 1D fields the angle $\theta = 0$ or π, and restricting variation to the z direction, this reduces to

$$f < 0 \iff \frac{\kappa_S}{\kappa_T} < R_\rho < 1, \tag{13}$$

which is a well known criterion for up-gradient buoyancy flux in double diffusive fluids (Veronis 1965; St. Laurent and Schmitt 1999).

b. Criterion for convection

The cold, low mechanical forcing simulation 2B shows a positive turbulent buoyancy flux (Figure 3) despite a horizontally-averaged density profile increasing with depth (Figure 2) at late times, i.e. the turbulent buoyancy flux is up-gradient. In this setting, convection is forced by preferential diffusion of temperature over salinity into fluid parcels near the ice/ocean boundary, causing increased density and forcing parcels to descend into the turbulent region below. In some cases this leads to a gravitationally unstable mean density profile. However, as case 2B shows, convection can also occur when the mean density profile is stably stratified. The positive buoyancy flux in case 2B is an example of an energy transfer from BPE to APE. Below, we examine this in detail by calculating the local diapycnal buoyancy flux.

To understand the influence of turbulence on the criterion for a negative diapycnal buoyancy flux, it is useful to consider the full 3D temperature and salinity fields. Figure 8 shows a scatter plot of the diapycnal buoyancy flux calculated from a 3D snapshot of the scalar fields for cases 1B, 1C, 2B and 2C, in (G_ρ, θ) space. Here the criterion in Eq.11 is exact and plotted as a black line. Also plotted is the diapycnal flux averaged for constant G_ρ. For $G_\rho < \kappa_S/\kappa_T$, the averaged diapycnal buoyancy flux $\langle \nabla b_p \cdot \hat{n} \rangle_{G_\rho}$ is dominated by large positive values and $\theta \simeq \pi$. These points are located in the salinity sublayer, where ∇T and ∇S are nearly vertical. For other values of G_ρ, the points are spread across all angles θ. This shows the role of turbulence in distorting temperature and salinity contours. In the non-convecting case 2C, there is scatter in θ even for $G_\rho < \kappa_S/\kappa_T$. In case 2B convection is weak but active and $\langle w'b' \rangle$ is up-gradient as the density profile is a monotonic function of height at the time shown. Here, the turbulent scatter is primarily restricted to the range $\kappa_S/\kappa_T < G_\rho < 1$.

The points within the sublayer with $\theta \sim \pi$ are split into points with positive and negative diapycnal buoyancy flux. Close to the boundary $G_\rho \sim R_\rho < \kappa_S/\kappa_T$ and salinity forms the largest contribution to the buoyancy flux and buoyancy gradient. Farther from the boundary $G_\rho \sim R_\rho > \kappa_S/\kappa_T$ and temperature makes a larger contribution to the buoyancy flux whilst salinity still contributes most to the buoyancy gradient, leading to an up-gradient buoyancy flux. In the convecting cases

1B and 1C, the 1D criterion $\kappa_S/\kappa_T < R_\rho < 1$ for an up-gradient buoyancy flux is sufficient to explain the averaged profile $\langle \nabla b_p \cdot \hat{n} \rangle_{G_\rho}$ if we take $G_\rho \sim R_\rho$. However, in the marginally convecting case 2B, the 3D criterion is necessary to explain the positive average diapycnal buoyancy flux for $0.2 < G_\rho < 1$ and in the non-convecting case 2C, the 1D approximation of $G_\rho \sim R_\rho$ performs poorly.

Figure 9 shows profiles of horizontally-averaged gradient ratio, scalar angle and diapycnal buoyancy flux from a convective simulation (case 1B) and a non-convective simulation (case 2C) as a function of depth in the upper 20 cm at $t = 30$ hrs. Shading indicates one standard deviation about the horizontal average. The depth where $\langle G_\rho \rangle = \kappa_S/\kappa_T$ is indicated with a blue dotted line, and the depths where $\langle \cos\theta \rangle = -1$ and $\langle \cos\theta \rangle = \cos\theta_c$ are indicated with red dashed lines. At the ice base, the gradient ratio will always be less than κ_S/κ_T as argued in Section 2b. Farther from the ice, the temperature gradient exceeds the salinity gradient giving $\langle G_\rho \rangle > \kappa_S/\kappa_T$. The convective simulation shows significant negative diapycnal buoyancy flux in the region of $\langle G_\rho \rangle > \kappa_S/\kappa_T$ and $\langle \cos\theta \rangle < \cos\theta_c$ below the salinity sublayer and above the turbulent region. The critical angle θ_c is an exact bound on the local up-gradient diapycnal buoyancy flux. However it is not necessary that the horizontally-averaged value gives the bound we see in the convecting case since the 3D criterion (Eq. 11) is nonlinear. The negative diapcynal buoyancy flux peaks at the depth where $\langle \cos\theta \rangle = -1$ in all convecting simulations. Non-convecting simulations have a positive mean diapycnal buoyancy flux at all depths, and the depth at which $\langle \cos\theta \rangle = -1$ is above the depth at which $\langle G_\rho \rangle = \kappa_S/\kappa_T$. This implies that turbulence influences the distribution of angles θ in the region of $\langle G_\rho \rangle > \kappa_S/\kappa_T$ where otherwise it is possible to form an up-gradient diapycnal buoyancy flux.

Figure 9 suggests that convection can be described using the relative thickness of two regions. The first is the region of $\langle G_\rho \rangle < \kappa_S/\kappa_T$, where the diapycnal buoyancy flux will always be down-gradient. This region is determined to first order by the relative thickness of the temperature and salinity sublayers. The second is the region of $\langle\cos\theta\rangle = -1$, where turbulent velocities do not alter the temperature or salinity fields. When the second region is thicker than the first, there is a region where the scalar gradients ∇T and ∇S are vertical, and $\kappa_S/\kappa_T < R_\rho < 1$, leading to an up-gradient diapycnal buoyancy flux, which causes the release of BPE and subsequently double-diffusive convection. We can also identify the region of $\langle\cos\theta\rangle < \cos\theta_c$, where on average the angle between ∇T and ∇S is conducive to an up-gradient diapycnal buoyancy flux. Below this region, $\cos\theta > \cos\theta_c$, and we expect the horizontally-averaged diapycnal flux to be positive due to turbulent motions.

G_ρ and θ are combinations of three-dimensional scalar gradients, and measuring these quantities in the field would be very challenging. It would be useful to have an approximate criterion that involves measurable quantities. In our simulations, the $G_\rho < \kappa_S/\kappa_T$ region is well described by the 1D approximation $R_\rho < \kappa_S/\kappa_T$. Our simulations also show a strong monotonic relationship, in a statistically averaged sense, between the angle θ and a common metric for turbulence, the buoyancy Reynolds number,

$$Re_b = \frac{\varepsilon}{\nu N^2}, \tag{14}$$

where $N^2 = \partial b/\partial z$ is the buoyancy frequency. We calculate Re_b using horizontally averaged values for both ε and N^2. The buoyancy Reynolds number quantifies the extent of the inertial subrange of the energy spectrum i.e. the separation between the Kolmogorov scale (the scale below which viscous effects dominate) and the Ozmidov scale (the scale above which buoyancy effects dominate). The buoyancy Reynolds number has also been used to identify double diffusion in the open ocean (Inoue et al. 2007).

For $Re_b < 1$ the flow will be laminar (Smyth and Moum 2000), and hence we might expect $\cos\theta \simeq -1$. The region of $\cos\theta < \cos\theta_c$ is well described by $Re_b < 10$, so for simulations with a region of negative mean diapycnal buoyancy flux, this region is bounded by $Re_b = 10$. For $1 < Re_b < 10$ we can consider the flow very weakly turbulent, and for larger buoyancy Reynolds numbers $Re_b > 10$, we find the turbulence is sufficiently developed to give $\langle\cos\theta\rangle > \cos\theta_c$, causing a positive mean diapycnal buoyancy flux.

Figure 10 shows how the horizontal mean diapycnal buoyancy flux varies with G_ρ, θ, and Re_b. Each point was calculated from 2D slices of the scalar fields at regular intervals throughout the simulations. The 2D slices are taken throughout the simulated period for all of the simulations conducted (listed in Table 1), and the mean profiles from all the sampled times are plotted in Figure 10. For simulations with a density peak there are values of $Re_b < 0$, however the region of interest is adjacent to the ice base so only points above the density peak are included. The points are plotted in (G_ρ, θ) space, where the colouration denotes the magnitude of the diapycnal buoyancy flux. The left panel shows that the region with an up-gradient buoyancy flux (blue points) is mostly bounded by $\langle G_\rho\rangle > \kappa_S/\kappa_T$ and $\cos\theta < \cos\theta_c$, indicated using dashed lines. For the non-convecting simulations, there are points with positive diapycnal flux for $\langle\cos\theta\rangle < \cos\theta_c$ and $G_\rho > \kappa_S/\kappa_T$, which does not occur for the convecting simulations.

The right panel in Figure 10 plots the same data as the left panel, but now as a function of R_ρ and Re_b. The gradient ratio, G_ρ is a good approximation to the density ratio, R_ρ in the diffusive sublayer, but they differ in the turbulent region. In all simulations, $Re_b < 1$ adjacent to the ice, suggesting that the near-ice region is laminar. If turbulent eddies existed close to the ice they would feel the effect of the wall, however no such eddies occur due to the strength of the stratification. The points that lie within the region $R_\rho > \kappa_S/\kappa_T$ and $Re_b < 1$ have a negative diapycnal buoyancy flux and these points occur at the top of the boundary layer in the convecting simulations. This leads to the following hypothesis: Convection will occur at the melting ice-base if the depth at which $Re_b = 1$ is deeper than the depth at which $R_\rho = \kappa_S/\kappa_T$. In the next section we will use this criterion to extend our results to a wider range of parameters.

5. Discussion

The criterion for diffusive convection described in Section 4b allows us to extrapolate our results to a wider range of parameters. For example, given a temperature and salinity profile, we can find the dissipation rate ε required to give $Re_b = 1$ at the depth where $R_\rho = \kappa_S/\kappa_T$. In practice, field measurements of T/S profiles within the ice-shelf ocean boundary layer cannot yet resolve the diffusive sublayers, with reliable measurements limited to depths of $\mathscr{O}(10\,\mathrm{cm})$. However observations may be combined with assumptions and models to estimate the relative depths of $Re_b = 1$ and $R_\rho = \kappa_S/\kappa_T$. This provides an estimate for the dissipation rate above which turbulence suppresses diffusive convection.

In the absence of T/S profiles, we can estimate the conditions that will be favorable for diffusive convection by considering the development of diffusive boundary layers into a fluid with initially uniform temperature and salinity. The solution of the unsteady diffusion equations forced by the melt boundary condition was derived by Martin and Kauffman (1977). Since heat diffuses down faster than salt, the density profile will be initially unstable with the potential to trigger diffusive convection. Over time, the addition of fresh water from melting will deepen the haline sublayer, decreasing the salinity gradient, and so decreasing N^2 in the halocline at the depth where $R_\rho = \kappa_S/\kappa_T$. The reduction in N^2 increases Re_b. Once $Re_b > 1$ at the depth where $R_\rho = \kappa_S/\kappa_T$, turbulence begins to suppress the up-gradient buoyancy flux which maintains diffusive convection.

Given an initial temperature, salinity and dissipation rate, we can calculate the time taken for the diffusive solution to meet our criterion for the shutdown of convection. This time is shown in Figure 11 for a fixed salinity $S_\infty = 34.572$, matching our simulations, while varying the initial temperature, T_∞ (normalised by the freezing temperature $T_m = \lambda_1 S_\infty + \lambda_2 + \lambda_3 P$), and the rate of dissipation, ε. Note that the diffusive solution does not account for turbulent mixing of the temperature and salinity profiles, so the transition times will not be quantitatively accurate. However, the diffusive solution provides a point of comparison between different levels of thermal forcing and rates of dissipation.

The simulations listed in Table 1 are included in Figure 11 for comparison. Convecting simulations are marked with circles and non-convecting simulations are marked with crosses and can be separated using a transition time of $t = 1$ s. This indicates that the predicted transition time might be a useful way to distinguish between convecting and non-convecting states in terms of their bulk parameters. The parameter space suggested by the observations of Larsen C Ice Shelf (Davis and Nicholls 2019) and George VI Ice Shelf (Venables et al. 2014) as well as the parameter space explored in the shear-driven Large-Eddy Simulations of Vreugdenhil and Taylor (2019) (inferred from a law-of-the-wall scaling) are marked using dashed boxes. The parameter space for the Larsen C Ice Shelf observations and the LES cover relatively short transition times, indicating double-diffusive convection may not occur. However, the George VI Ice Shelf parameter space has a long transition time and hence the flow is amenable to transient double-diffusive convection as suggested by Kimura et al. (2015).

In the simulations and analysis here, we used idealised initial conditions with uniform temperature and salinity. However, diffusive convection can occur in other configurations. For example, consider a turbulent ice-ocean boundary layer in a non-convecting steady state. If turbulence levels decrease (e.g. due to weakening currents), the buoyancy Reynolds number will decrease, so the depth at which $Re_b = 1$ will increase. If this depth at which $Re_b = 1$ becomes deeper that the depth at which $R_\rho = \frac{\kappa_S}{\kappa_T}$ then the criterion from Section 4b is satisfied and convection will ensue. The double-diffusive convection preferentially transports heat over salt, so we would expect the salt boundary layer to grow slowly. Therefore a boundary layer in warm or weakly turbulent conditions may take a long time to adjust to modest changes in turbulence levels.

6. Conclusions

Motivated by observations made beneath George VI ice shelf in Antarctica, we conducted a series of numerical simulations of an idealised ocean boundary layer beneath a melting ice shelf. The simulations were initialised with constant salinity and temperature and the evolution of the system under a thickening salt sublayer was studied.

Two distinct flow regimes were observed. In one regime, the mean density profile increased with depth and the density field acted to damp the forced turbulence. This is the standard assumption in stratified melting ice-ocean boundary parameterisations. In the other regime, double-diffusive convection occurred and potential energy was converted into kinetic energy, forced by an up-gradient buoyancy flux in a region near the ice base. All simulations started in the convective regime, but some quickly transitioned to a turbulence-damping state. Simulations in different regimes exhibit qualitatively different patterns in the velocity field, melt rate and melt pattern.

We examined the influence of temperature and ambient turbulence levels on the flow regime by systematically varying the initial and far-field temperature and the strength of the mechanical forcing. A criterion for an up-gradient buoyancy flux and hence double-diffusive convection using the $3D$ scalar gradients (Middleton and Taylor 2020) was applied to the simulation data. This criterion identified the region of up-gradient diapycnal buoyancy flux near the ice base, responsible for convection.

We developed a simple prediction for an up-gradient buoyancy flux (Middleton and Taylor 2020) at the ice base based on local values of the density ratio and the buoyancy Reynolds number Re_b. We found double-diffusive convection if the depth of the region beneath the ice of $Re_b \lesssim 1$ is deeper than the region of $R_\rho \lesssim \kappa_S/\kappa_T$. We then used solutions from the unsteady diffusion equations from Martin and Kauffman (1977) to estimate when the boundary layer will be favourable to double-diffusive convection based on the turbulent dissipation rate and the far field temperature.

The interaction of melt-driven convection with thermohaline layering and anisotropic turbulence (including shear) could modify some of our conclusions, and in particular the specific value of the buoyancy Reynolds number used in the criterion for the shutdown of double-diffusive convection could be sensitive to the source of turbulence. This could be investigated in future studies. We anticipate that the principles used here to distinguish between externally-forced turbulence and double-diffusive convection could be applied to other settings and will be a useful starting point in future work.

Our results indicate that melt-driven double-diffusive convection can dominate the dynamics within the ice shelf-ocean boundary layer if the turbulence is sufficiently weak and/or the thermal driving is sufficiently large. This study suggests future ice-ocean boundary layer parameterisations may need to distinguish between convective and non-convective conditions in the melting regime. However, more observations in warm, weakly turbulent conditions are needed to assess the prevalence of double-diffusive convection beneath ice shelves.

Acknowledgements

This work was funded by grants from the Natural Environment Research Council, NE/N009746/1 and NE/N010027/1.

Appendix A: Grid Stretching

The Kolmogorov length scale gives a measure of the smallest turbulent eddies and is defined as

$$\eta = \left(\frac{\nu^3}{\varepsilon}\right)^{\frac{1}{4}} \tag{15}$$

We resolve the Kolmogorov scale within the 'observation region' of our domain ($z < 2.6$ m). The diffusivities for heat and salt are smaller than the diffusivity for momentum (i.e. kinematic viscosity ν), so variability on scales smaller than the Kolmogorov scale is possible. These scales are quantified using the thermal and haline Batchelor scales, defined as

$$l_B^T = \frac{\eta}{Pr^{\frac{1}{2}}} = \left(\frac{\nu \kappa_T^2}{\varepsilon}\right)^{\frac{1}{4}}, \qquad l_B^S = \frac{\eta}{Sc^{\frac{1}{2}}} = \left(\frac{\nu \kappa_S^2}{\varepsilon}\right)^{\frac{1}{4}}. \tag{16}$$

Figure 12 shows the grid spacing graphically, comparing the distance between grid points Δz to the Kolmogorov and Batchelor scales, calculated based on the dissipation rate profile of the passive spin up. We have compared our grid spacing to the turbulent length scales multiplied by a factor of 2 as a commonly argued factor.

Vreugdenhil and Taylor (2018) found that including 7 grid points within the conducting sublayer was sufficient to resolve the diffusive fluxes at the wall in their simulations of stratified plane Couette flow, a criterion which was then applied to resolve salt fluxes in the ice-ocean boundary layer simulations of Vreugdenhil and Taylor (2019)). We use the same criterion here, and we have further verified that our simulations follow the analytical diffusive solution (see Figure 2) at early times, before turbulent mixing increases the haline sublayer thickness. Using the definition of the salinity sublayer as when the salinity reaches 99% of its far field value, we find that, for the diffusive solution, we have 7 grid points within the haline sublayer after $t = 25$ minutes. Before this time, the simulated scalar fields match the diffusive solution which suggests the scalar fluxes are resolved at the boundary throughout our simulations.

References

Begeman, C. B., and Coauthors, 2018: Ocean stratification and low melt rates at the Ross Ice Shelf grounding zone. *Journal of Geophysical Research: Oceans*, **123 (10)**, 7438–7452.

Carpenter, J. R., T. Sommer, and A. Wüest, 2012: Simulations of a double-diffusive interface in the diffusive convection regime. *Journal of Fluid Mechanics*, **711**, 411–436.

Crapper, P., 1976: Fluxes of heat and salt across a diffusive interface in the presence of grid generated turbulence. *International Journal of Heat and Mass Transfer*, **19 (12)**, 1371–1378.

Davis, P. E., and K. W. Nicholls, 2019: Turbulence observations beneath Larsen C Ice Shelf, Antarctica. *Journal of Geophysical Research: Oceans*, **124 (8)**, 5529–5550.

Frank, F. C., 1950: Radially symmetric phase growth controlled by diffusion. *Proceedings of the Royal Society A: Mathematical, Physical and Engineering Sciences*, **201 (1067)**, 586–599.

Gade, H. G., 1979: Melting of ice in sea water: A primitive model with application to the antarctic ice shelf and icebergs. *Journal of Physical Oceanography*, **9 (1)**, 189–198.

Gayen, B., R. W. Griffiths, and R. C. Kerr, 2016: Simulation of convection at a vertical ice face dissolving into saline water. *Journal of Fluid Mechanics*, **798**, 284–298.

Guthrie, J. D., J. H. Morison, and I. Fer, 2013: Revisiting internal waves and mixing in the arctic ocean. *Journal of Geophysical Research: Oceans*, **118 (8)**, 3966–3977.

Hickel, S., N. Adams, and N. Mansour, 2007: Implicit subgrid-scale modeling for large-eddy simulation of passive-scalar mixing. *Physics of Fluids*, **19 (9)**, 095 102.

Holland, D. M., and A. Jenkins, 1999: Modeling thermodynamic ice–ocean interactions at the base of an ice shelf. *Journal of Physical Oceanography*, **29 (8)**, 1787–1800.

Holland, P. R., A. Jenkins, and D. M. Holland, 2010: Ice and ocean processes in the Bellingshausen sea, Antarctica. *Journal of Geophysical Research: Oceans*, **115 (5)**, 1–16.

Inoue, R., H. Yamazaki, F. Wolk, T. Kono, and J. Yoshida, 2007: An estimation of buoyancy flux for a mixture of turbulence and double diffusion. *Journal of physical oceanography*, **37 (3)**, 611–624.

Jenkins, A., K. W. Nicholls, and H. F. Corr, 2010: Observation and parameterization of ablation at the base of Ronne Ice Shelf, Antarctica. *Journal of Physical Oceanography*, **40 (10)**, 2298–2312.

Keitzl, T., J. P. Mellado, and D. Notz, 2016: Reconciling estimates of the ratio of heat and salt fluxes at the ice–ocean interface. *Journal of Geophysical Research: Oceans*, **121 (12)**, 8419–8433.

Kimura, S., K. W. Nicholls, and E. Venables, 2015: Estimation of ice shelf melt rate in the presence of a thermohaline staircase. *Journal of Physical Oceanography*, **45 (1)**, 133–148.

Martin, S., and P. Kauffman, 1977: An experimental and theoretical study of the turbulent and laminar convection generated under a horizontal ice sheet floating on warm salty water. *Journal of Physical Oceanography*, **7 (2)**, 272–283.

McPhee, M. G., G. A. Maykut, and J. H. Morison, 1987: Dynamics and thermodynamics of the ice/upper ocean system in the marginal ice zone of the Greenland Sea. *Journal of Geophysical Research: Oceans*, **92 (C7)**, 7017–7031.

Merryfield, W. J., 2000: Origin of thermohaline staircases. *Journal of Physical Oceanography*, **30 (5)**, 1046–1068.

Middleton, L., and J. Taylor, 2020: A general criterion for the release of background potential energy through double diffusion. *Journal of Fluid Mechanics*.

Orszag, S. A., 1971: On the elimination of aliasing in finite-difference schemes by filtering high-wavenumber components. *Journal of the Atmospheric sciences*, **28 (6)**, 1074–1074.

Phillips, O., 1972: Turbulence in a strongly stratified fluid—is it unstable? *Deep Sea Research and Oceanographic Abstracts*, Elsevier, Vol. 19, 79–81.

Radko, T., 2013: *Double-Diffusive Convection*. Cambridge University Press.

Rao, K., and S. de Bruyn Kops, 2011: A mathematical framework for forcing turbulence applied to horizontally homogeneous stratified flow. *Physics of Fluids*, **23 (6)**, 065 110.

Rignot, E., S. Jacobs, J. Mouginot, and B. Scheuchl, 2013: Ice-shelf melting around Antarctica. *Science*, **341 (6143)**, 266–270.

Scalo, C., U. Piomelli, and L. Boegman, 2012: Large-eddy simulation of oxygen transfer to organic sediment beds. *Journal of Geophysical Research: Oceans*, **117 (C6)**.

Shibley, N., and M.-L. Timmermans, 2019: The formation of double-diffusive layers in a weakly turbulent environment. *Journal of Geophysical Research: Oceans*, **124 (3)**, 1445–1458.

Smyth, W. D., and J. N. Moum, 2000: Length scales of turbulence in stably stratified mixing layers. *Physics of Fluids*, **12 (6)**, 1327–1342.

St. Laurent, L., and R. Schmitt, 1999: The contribution of salt fingers to vertical mixing in the North Atlantic Tracer Release Experiment. *Journal of Physical Oceanography*, **29 (7)**, 1404–1424.

Taylor, J., S. de Bruyn Kops, C. Caulfield, and P. Linden, 2019: Testing the assumptions underlying ocean mixing methodologies using direct numerical simulations. *Journal of Physical Oceanography*, **49 (11)**, 2761–2779.

Taylor, J. R., 2008: Numerical simulations of the stratified oceanic bottom boundary layer. Ph.D. thesis, UC San Diego.

Taylor, J. R., and R. Stocker, 2012: Trade-offs of chemotactic foraging in turbulent water. *Science*, **338 (6107)**, 675–679.

Turner, J., 1968: The behaviour of a stable salinity gradient heated from below. *Journal of Fluid Mechanics*, **33 (1)**, 183–200.

Venables, E., K. Nicholls, F. Wolk, K. Makinson, and P. Anker, 2014: Measuring turbulent dissipation rates beneath an Antarctic ice shelf. *Marine Technology Society Journal*, **48 (5)**, 18–24.

Veronis, G., 1965: On finite amplitude instability in thermohaline convection. *J. mar. Res*, **23 (1)**, 1–17.

Vreugdenhil, C. A., and J. R. Taylor, 2018: Large-eddy simulations of stratified plane couette flow using the anisotropic minimum-dissipation model. *Physics of Fluids*, **30 (8)**, 085 104.

Vreugdenhil, C. A., and J. R. Taylor, 2019: Stratification effects in the turbulent boundary layer beneath a melting ice shelf: Insights from resolved large-eddy simulations. *Journal of Physical Oceanography*, **49 (7)**, 1905–1925.

Wang, L.-P., S. Chen, J. G. Brasseur, and J. C. Wyngaard, 1996: Examination of hypotheses in the Kolmogorov refined turbulence theory through high-resolution simulations. part 1. velocity field. *Journal of Fluid Mechanics*, **309**, 113–156.

Winters, K. B., P. N. Lombard, J. J. Riley, and E. A. D'Asaro, 1995: Available potential energy and mixing in density-stratified fluids. *Journal of Fluid Mechanics*, **289**, 115–128.

LIST OF TABLES

Run	Mean Forced Dissipation ε_0 ($\mathrm{m^2 s^{-3}}$)	T_∞ (°C)	ΔT (°C)	ΔS (ppt)	Turbulent Buoyancy Flux $\langle w'b' \rangle$	Density Ratio $R_\rho = \frac{\beta \Delta S}{\alpha \Delta T}$
1A	No Forcing	0.15	1.49	14.4	3.5×10^{-9}	197
1B	$(8.7 \pm 1.8) \times 10^{-11}$	0.15	1.43	15.4	2.3×10^{-9}	220
1C	$(1.7 \pm 0.15) \times 10^{-9}$	0.15	1.43	15.5	2.2×10^{-9}	220
2A	No Forcing	-2.15	5.8×10^{-3}	9.64×10^{-2}	6.0×10^{-12}	338
2B	$(8.7 \pm 1.8) \times 10^{-11}$	-2.15	5.4×10^{-3}	10.3×10^{-2}	5.1×10^{-12}	383
2C	$(1.7 \pm 0.15) \times 10^{-9}$	-2.15	5.9×10^{-3}	9.46×10^{-2}	-3.4×10^{-11}	325
3	$(8.7 \pm 1.7) \times 10^{-11}$	-2.16	7.3×10^{-4}	1.04×10^{-2}	-5.2×10^{-14}	293
4	$(8.7 \pm 1.7) \times 10^{-11}$	-2.161	1.8×10^{-4}	2.47×10^{-3}	-5.4×10^{-13}	274
5	$(8.7 \pm 1.7) \times 10^{-11}$	-2.1613	1.5×10^{-5}	1.81×10^{-4}	-8.7×10^{-14}	242
6	$(8.7 \pm 1.7) \times 10^{-11}$	-2.161325	4×10^{-7}	4.00×10^{-6}	-1.4×10^{-15}	220

TABLE 1. Table of simulation runs. Values for ΔT, ΔS, and R_ρ are averaged across the simulation. The turbulent vertical buoyancy flux $\langle w'b' \rangle$ is averaged across the simulation for depths 0.1 m $< z <$ 2.6 m for the first 35 hrs to enable comparison across simulations run for different lengths of time. Simulations above the dotted line are convecting throughout the simulated time, and those below are not.

LIST OF FIGURES

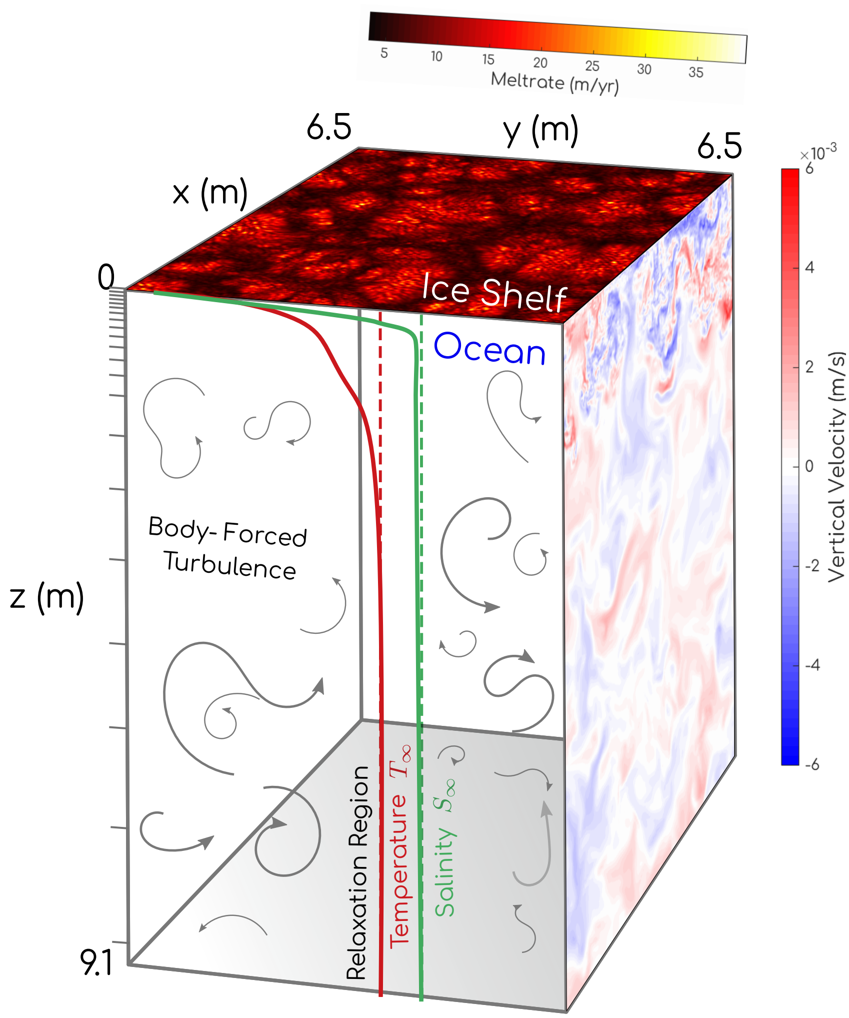

FIG. 1. Schematic of model domain with included snapshots of vertical velocity field and melt rate for warm, low mechanical forcing simulation 1B listed in Table 1.

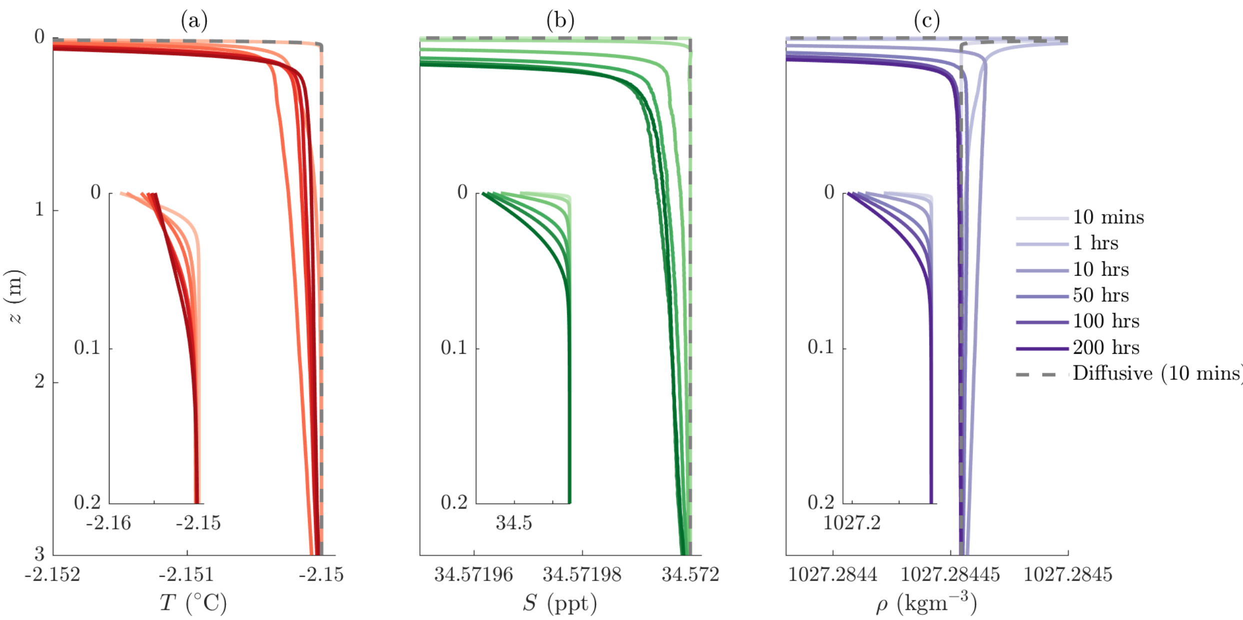

FIG. 2. Horizontally-averaged temperature (a), salinity (b) and density (c) averaged over an hour, at hours $1, 10, 50, 100$ and 200 for the cold, low mechanical forcing simulation 2B. Additionally we have shown the diffusive solution profiles (Martin and Kauffman 1977) and the simulation profiles at $t = 10$ mins which compare well. The inset shows the upper 20 cm in each panel, showing the full variation in the scalars.

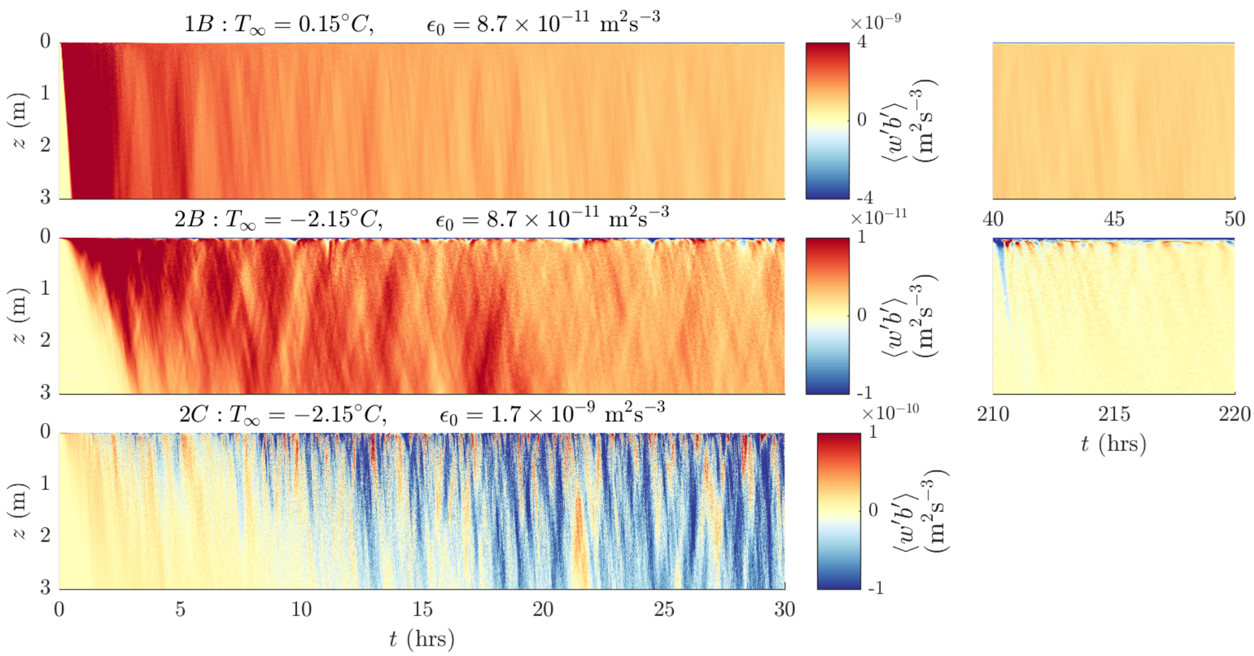

FIG. 3. Time evolution of the horizontally-averaged turbulent buoyancy flux $\langle w'b' \rangle$ for simulation runs 2B (cold,low mechanical forcing), 2C (cold, high mechanical forcing) and 1B (warm, high mechanical forcing). Positive values signify stratification acting to transfer available potential energy to turbulent kinetic energy and negative values indicate stratification acting to transfer turbulent kinetic energy into available potential energy. First 30 hours of each simulation are shown concurrently, then later times are shown for simulations 1A and 2B.

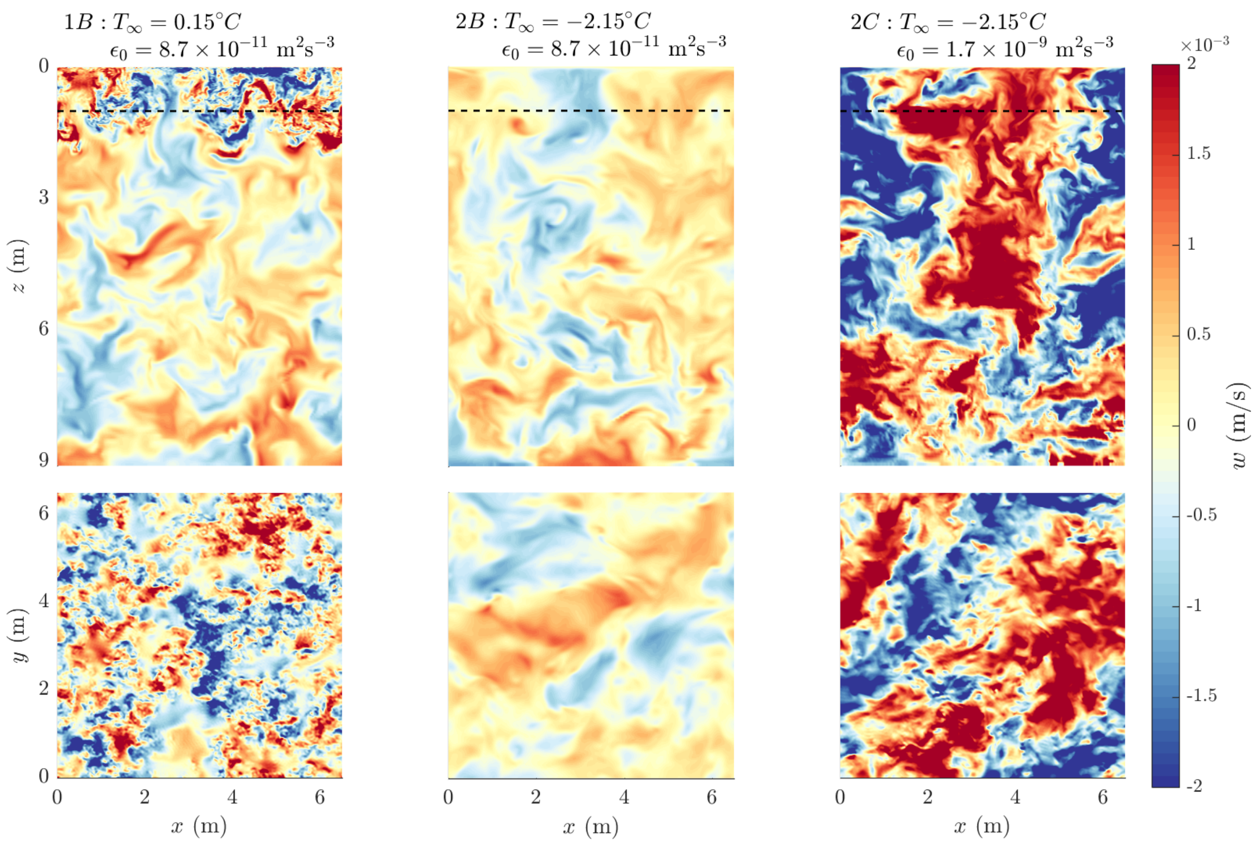

FIG. 4. Vertical velocity slices at $t = 1$ hr for simulation runs 2B (cold,low mechanical forcing), 2C (cold, high mechanical forcing) and 1B (warm, high mechanical forcing). All plots are on the same color scale to illustrate relative magnitudes of vertical velocities. Horizontal slices (lower panels) taken at 1m depth (location shown with dotted line in upper panels).

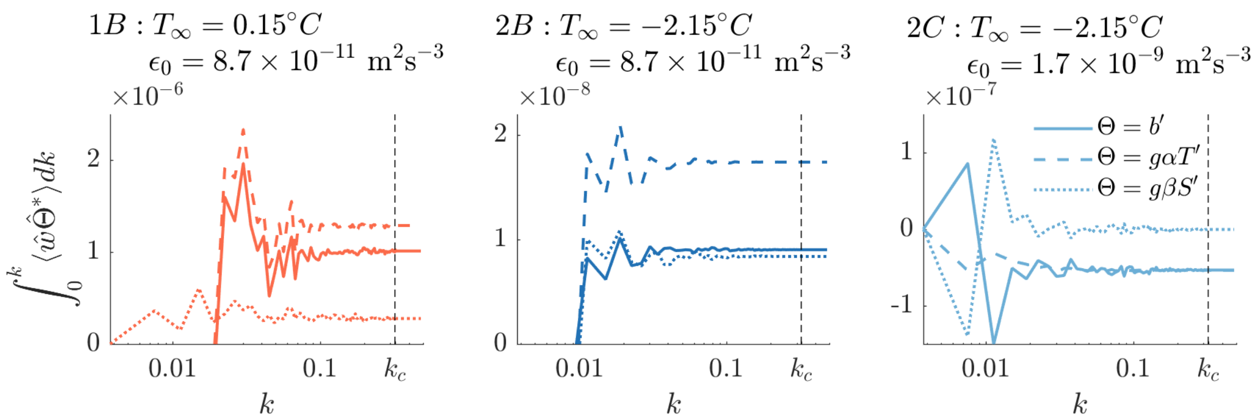

FIG. 5. Turbulent flux of temperature, salinity and buoyancy, averaged between 1 m and 3 m depth, integrated in Fourier space up to wavenumber k. Values taken from 3D fields at $t = 1$ hr for simulation runs 2B (cold,low mechanical forcing), 2C (cold, high mechanical forcing) and 1B (warm, high mechanical forcing) as in Figure 4. The Fourier transform is denoted using $\hat{\cdot}$ and the complex conjugate is denoted by *. The wavenumber $k = \sqrt{k_x^2 + k_y^2}$ is the horizontal radial wavenumber. Values of the integral $\int_0^k \langle \hat{w}\hat{\Theta}^* \rangle dk$ converge for $\Theta = b', g\alpha T', g\beta S'$ with increasing wavenumber, suggesting the resolution is sufficient to capture the scalar fluxes. The cutoff frequency k_c used in the $\frac{2}{3}$ de-aliasing rule is included as a dashed vertical line.

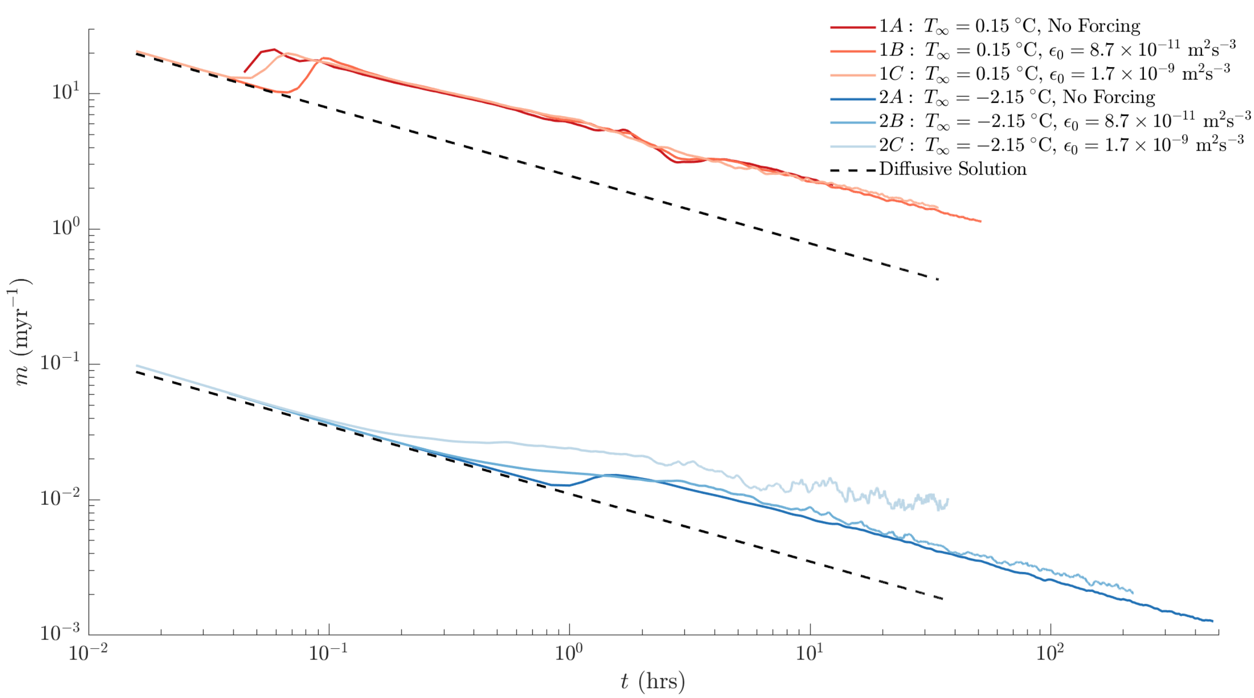

FIG. 6. Melt rate for cases 1A, 1B, 1C (the relatively warm cases) and for cases 2A, 2B, 2C (the relatively cold cases). The diffusive solution (Martin and Kauffman 1977) is shown in a dotted line for both warm and cold cases.

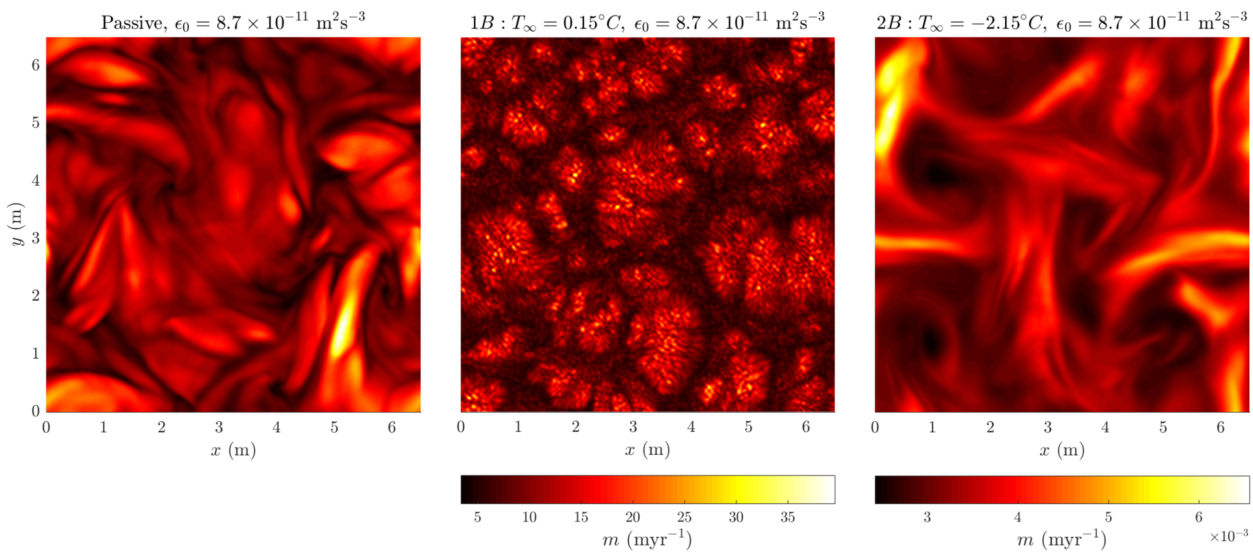

FIG. 7. Horizontal melt rate patterns for cases 1B and 2B. Snapshots taken at the same time as in Figure 4. Also included snapshot from the passive spin up simulation to compare patterning (melt rate values are inflated in this case due to lack of stable haline sublayer, so not included).

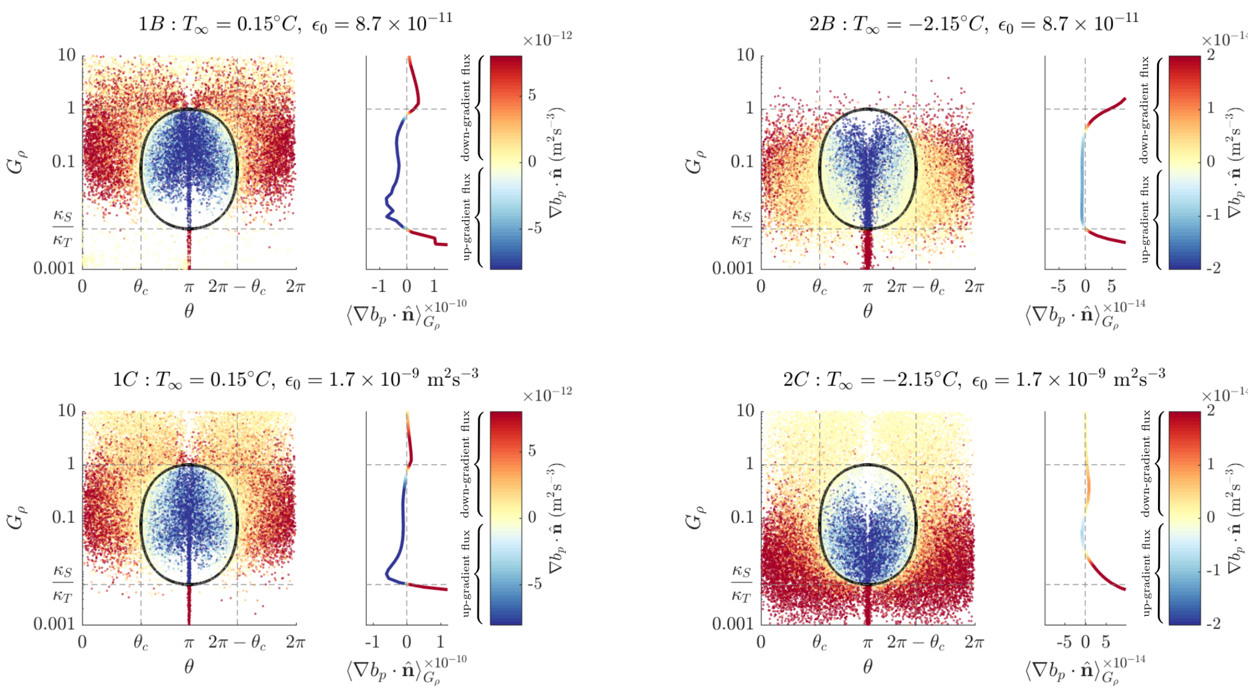

FIG. 8. Diapycnal buoyancy flux (color) for relatively warm cases 1B and 1C and relatively cold cases 2B and 2C. 3D gradients are used to compute the diapycnal flux, $\nabla b_p \cdot \hat{\boldsymbol{n}}$, the gradient ratio $G_\rho = \frac{\alpha|\nabla T|}{\beta|\nabla S|}$ and the angle θ between $-\nabla T$ and ∇S. A random set of $^1/_{1000}{}^{th}$ of the points are then plotted as a scatter graph in (G_ρ, θ) space, coloured by the diapycnal flux. The line $f(G_\rho, \theta) = 0$ is plotted in black and divides the negative values of diapycnal flux (up-gradient) on the inside of the line from the positive (down-gradient) values outside of the line. To the right of each scatter plot is an average over the diapycnal flux across G_ρ i.e. $\langle \nabla b_p \cdot \hat{\boldsymbol{n}} \rangle_{G_\rho}$, on the same colour bar as the scatter plot. Note the gradient ratio G_ρ is on a log scale.

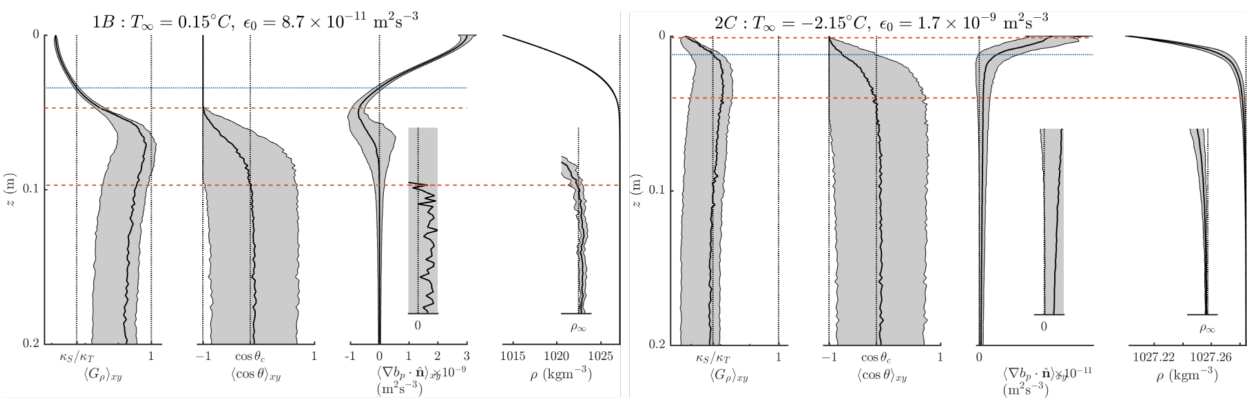

FIG. 9. Vertical profiles of the gradient ratio G_ρ, the scalar angle $\cos\theta$, the diapycnal flux $\nabla b_p \cdot \hat{\boldsymbol{n}}$ and the density ρ in the upper 20 cm of a convecting simulation (warm, low mechanical forcing case 1B) and a non-convective simulation (cold, high mechanical forcing case 2C) at $t = 30$ hrs. The spatial mean is shown in solid with one spatial standard deviation denoted by the shaded region. The dashed lines denote the depths at which $\langle\cos\theta\rangle_{xy} = -1$ and $\langle\cos\theta\rangle_{xy} = \cos\theta_c$. The dotted line denotes the depth at which $\langle G_\rho\rangle_{xy} = \frac{\kappa_S}{\kappa_T}$. The insets are a close up version of the adjacent profiles on the same z axis. The far-field density is denoted with a vertical dashed line in the plot of ρ. Note the gradient ratio G_ρ in the left panel is on a log scale.

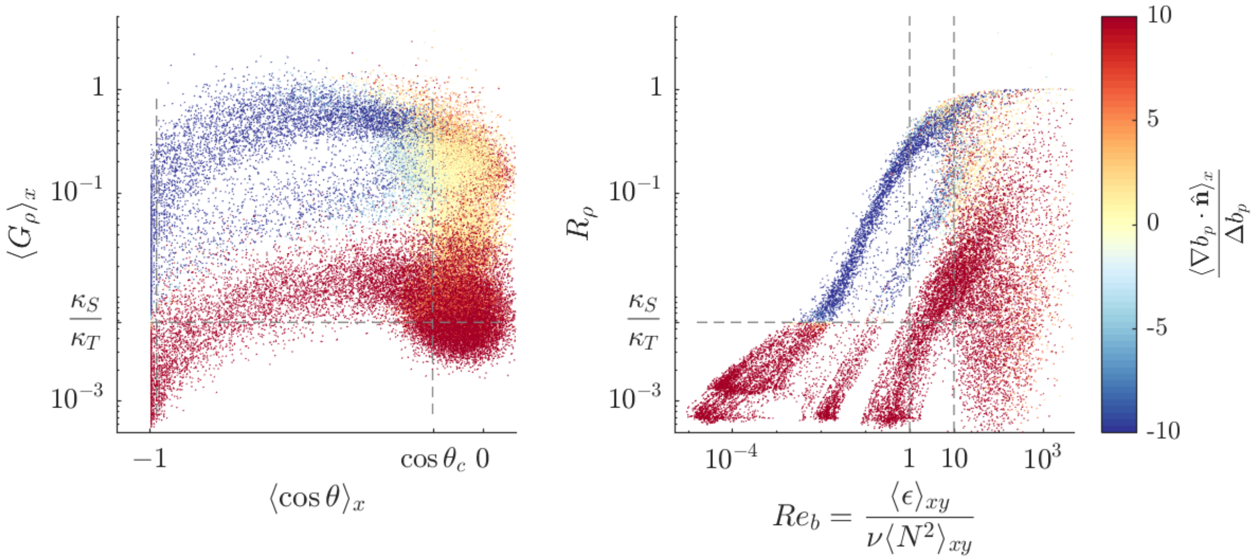

FIG. 10. Diapycnal buoyancy flux (color) for cases 1-6 in Table 1 plotted in (G_ρ, θ) (left) and in (R_ρ, Re_b) space (right). The diapycnal buoyancy flux is normalised by the maximum (i.e. initial) difference $\Delta b_p = b_p^{\text{bottom}} - b_p^{\text{top}}$ across each simulation for comparison. The points were sampled from 2D *x*-*z* slices extracted from the 3D simulations at regular intervals.

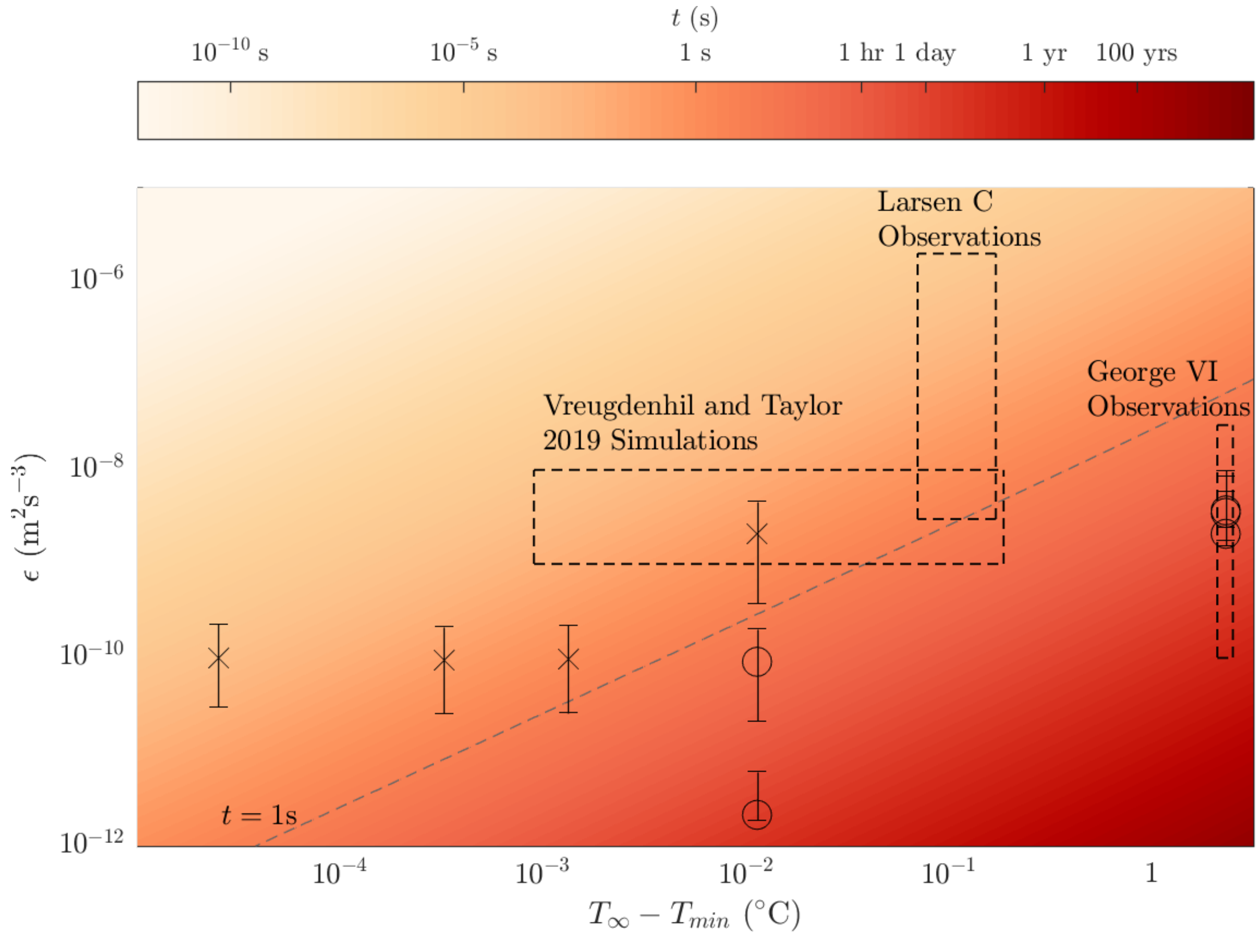

FIG. 11. Predicted time required for the system to transition from diffusive convection to stratified turbulence, calculated with the diffusive solution (Martin and Kauffman 1977) with far field temperature T_∞ and prescribed turbulent dissipation rate, ε. 'Transition' occurs when $Re_b = 1$ at $R_\rho = \kappa_S/\kappa_T$. The far-field salinity $S_\infty =$ 34.572 ppt in all cases and $T_{min} = \lambda_1 S_\infty + \lambda_2 + \lambda_3 P$ is the freezing temperature. Simulation values of $\varepsilon_{measured}$ are given by markers with bounds indicating maximum and minimum values. Circular markers indicate convecting simulations and cross markers indicate non-convecting simulations. The contour for diffusive solutions to take $t = 1$ s to transition is marked as a dividing point between the convecting and non-convecting simulations. Regions of parameter space occupied by the observations from Larsen C Ice Shelf (Davis and Nicholls 2019), George VI Ice Shelf (Venables et al. 2014), and the LES for a shear driven boundary layer (Vreugdenhil and Taylor 2019) shown with dashed boxes.

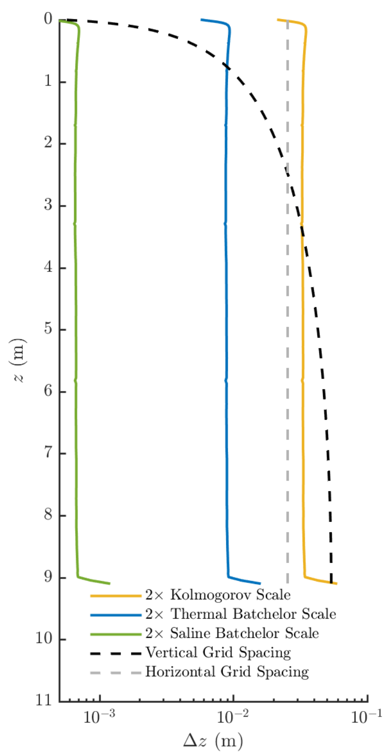

FIG. 12. Grid spacing plotted with depth. Kolmogorov and Batchelor scales for both scalars are shown, with dissipation rates taken from passive simulation for $\varepsilon_0 = 8.7 \times 10^{-11}\mathrm{m}^2\mathrm{s}^{-3}$.